Annals of Nuclear Energy 36 (2009) 1597–1613

Contents lists available at ScienceDirect

Annals of Nuclear Energy

journal homepage: www.elsevier.com/locate/anucene

Two-dimensional interaction of oxidic corium with concretes: The VULCANO VB test series

Christophe Journeau [a,*], Pascal Piluso [a], Jean-François Haquet [a], Eric Boccaccio [a], Valérie Saldo [a], Jean-Michel Bonnet [a,1], Sophie Malaval [a], Laure Carénini [a,1], Laurent Brissonneau [b]

[a] CEA, DEN, STRI/LMA, Cadarache, F-13108 St Paul lez Durance, France
[b] CEA, DEN, STPA/LPC, Cadarache, F-13108 St Paul lez Durance, France

ARTICLE INFO

Article history:
Received 16 October 2008
Received in revised form 6 July 2009
Accepted 7 July 2009
Available online 26 August 2009

ABSTRACT

Three two-dimensional Molten Core–Concrete Interaction tests have been conducted in the VULCANO facility with prototypic oxidic corium. The major finding is that for the two tests with silica-rich concrete, the ablation was anisotropic while it was isotropic for limestone-rich concrete. The cause of this behaviour is not yet well understood.

Post Test Examinations have indicated that for the silica-rich concrete, the corium melt mixed specifically with mortar, while, for limestone-rich concretes, the analysed samples were in accordance with a corium–concrete mixing. The experimental results are described and compared to numerical codes. Separate Effect Tests with Artificial Concretes and prototypic corium are proposed to understand the phenomena governing the ablation geometry.

1. Introduction

In the hypothetical case of a nuclear reactor severe accident, the core could melt and form a molten pool called corium. It could eventually melt through the vessel and interact with the pit concrete. So, corium is composed of uranium oxide, partly or totally oxidized zirconium, steel and its oxides, fission products, and is mixing with concrete decomposition products in the reactor pit. In current PWRs, this concrete basemat is the ultimate barrier, while in the EPR (Fischer, 2004), the reactor pit provides temporary melt retention before spreading in the core catcher.

It is reminded that concrete is a multiphase material made of a mix of cement, water, sand and gravel. For the behaviour of concrete at high temperatures, the European standard dedicated to the structural fire design of concrete structures (AFNOR, 2001) considers three types of concretes depending on the nature of the aggregates (sand and gravel): siliceous aggregates, limestone aggregates and light aggregates. For nuclear reactors of the first and second generations, the choice of the reactor pit concrete was mainly made on criteria of mechanical strength, durability and cost, without taking into account any consideration about hypothetical severe accidents. Several compositions of concretes have been reported depending mainly on the nature of the sand and gravel used in the concrete mixture: siliceous and basaltic concretes (Shin et al., 2002; Farmer, 2007), limestone concretes (Farmer, 2007) as well as concrete with mixed aggregates of limestone and silica (Journeau et al., 2007a) at various proportions. For third generation reactors such as the EPR, a dedicated concrete containing silicon and iron oxides has been designed (Azarian et al., 2004).

Molten Core–Concrete Interaction (MCCI) is characterized by intense coupling of many complicated phenomena, such as: high temperature concrete behaviour and its decomposition; thermal hydraulics and heat transfer of the corium pool agitated by gas bubbles; physico-chemistry of the multi-component corium melt with a continuously-changing composition due to the admixture of molten concrete, and wide solidification ranges (of the order of 1000 K); oxidation of metals; and partial solidification of the melt and the behaviour of slurries or interfacial crusts. Identification and quantification of these phenomena with respect to their importance for accident analysis requires an iterative process of integral experiments, separate effect tests, and development of models and their verification.

Experiments on MCCI started in the 1980s (Alsmeyer et al., 1995). Although numerous Molten Core–Concrete Interaction experiments have already been performed, there are still large uncertainties mainly on the two-dimensional profiles of the ablation velocity and on the effect of the metallic layer. These issues have thus been classified with a high priority by the SARNET Severe Accident Research Priorities Group (Trambauer and Schwinges, 2007). The VULCANO VB test series has been devoted to the study of long-term 2D interaction of corium with concretes of different prototypical compositions. The presented oxidic corium–concrete tests have been conducted in the same period as the OCDE/MCCI tests (Farmer, 2007). Performing two test series with different

* Corresponding author. Tel.: +33 4 42 25 41 21; fax: +33 4 42 25 77 88.
E-mail address: christophe.journeau@cea.fr (C. Journeau).
[1] Currently with IRSN (Institut de Recherche et de Sûreté Nucléaire).

0306-4549/$ - see front matter © 2009 Elsevier Ltd. All rights reserved.
doi:10.1016/j.anucene.2009.07.006

Nomenclature

C	concentration
c_p	specific heat
D	diffusion coefficient
F	heat flux
F_a	heat flux from the corium pool
g	acceleration of gravity
H	enthalpy, heat of fusion
h	thickness
k	thermal conductivity
Q	extracted heat
R	radius
T	temperature
U	velocity
V_i	dissolution rate
V_{Si}	silica gravel melting rate
Z	curvilinear abscissa

Greek Letters

β	angular position
κ	thermal diffusivity
μ	dynamic viscosity
ρ	density
τ	characteristic time

Subscripts

0	liquid corium
1	during remelting phase
c	corium crust
cm	crust–molten concrete interface
i	interface
liq	liquidus
m	molten concrete
s	solid concrete
Si	silica gravel

geometries and heating technologies enabled to significantly lower the probability of experimental artifact.

A first section is devoted to summarizing the previous MCCI tests and presenting their major learning. In the next section, the VULCANO facility and the VB test series will be described. The subsequent section will be devoted to material aspects. Then modeling of corium–concrete interaction will be discussed. Finally, the major differences between limestone-rich and silica-rich concretes will be analysed.

2. Summary of other MCCI experimental programs

Table 1 summarizes the major experiments that were conducted in the early days of MCCI research, mostly with either high temperature simulant oxides (BETA, WETCOR) or prototypic UO_2-based melts (ACE/MACE, SURC). Most of these experiments use an electrical heating technique to simulate the internal decay heat and to allow studies of long-term behaviour, either induction heating, or direct resistance heating. Except for the 2D BETA experiments, all of these were devoted to 1D geometries. An overview of these tests and their use in code development and application was provided by Alsmeyer et al. (1995).

These tests showed that thermal ablation was the major process governing MCCI: The ablation rate is, at the first order, the ratio of the heat flux F to the enthalpy needed to heat and melt a unit volume of concrete:

$$v = \frac{F}{\rho(H_{\text{concrete melting}} - H_0)} \quad (1)$$

After a first intense period of interaction upon melt release, controlled by the initial melt overheat and the zirconium oxidation processes, the typical long time erosion rates are several centimetres per hour. During some of these tests, the power was doubled at once (in view of destroying an anchored crust) and the pool temperature varied only slightly. This indicates that for the given conditions the temperature of the melt is close to the interface temperature, so that a doubling of the temperature difference (accounting for a doubling of the heat flux at almost constant heat transfer coefficient) remains within the temperature measurement uncertainties. This confirmed the so-called coupled approach (Seiler and Froment, 2000) in which the heat transfer coefficient are large and the temperature difference between pool and interface is small.

All experiments show the strong release of gases bubbling through the melt and generating a well-stirred melt pool. The resulting gases are H_2 and CO, which may reach flammable concentrations. In some tests, eruptions of gas-entrained corium have been observed that formed debris-piles like volcanoes. The ACE/MACE tests also provided valuable information on the aerosol release by oxidic corium during the interaction: Only a small fraction is released, especially above siliceous concretes.

The 2D BETA experiments showed pronounced axial erosion through the metal phase, depending on the power generated in the melt (in the heavier metallic layer, whereas less than 20% of the decay heat is actually generated in the metallic phase of corium). This result must not be directly applied to the oxidic melt behaviour but requires careful consideration of the fact that heat was provided in the metal and of the different transport properties of the oxide.

Table 1
Early MCCI experimental programs.

Program	Lab.	Concrete	Corium	Scale (pool volume)	Geometry	Parameters
BETA (Alsmeyer et al., 1995)	FZ Karlsruhe (Germany)	Siliceous, limestone	Simulant (Al_2O_3 + CaO + Fe)	~100 L	2D	Decay power (induction). Melt mass 60–120 min
ACE (Thompson et al., 1997)	Argonne National Lab. (USA)	Siliceous, limestone, limestone–common sand	Oxide	40 L	1D	Decay power (direct current). Corium composition 30–120 min
SURC (Copus et al., 1989, 1990, 1992)	Sandia Nat. Lab. (USA)	Siliceous, limestone	Oxide (incl. some Zr and FPs)	~25 L	1D	Induction heating. 120–180 min. Aerosol release
WETCOR (Blose et al., 1993)	Sandia Nat. Lab. (USA)	Limestone–common sand	Alumina based simulant	15 L	1D	Overlying water pool 120 min
MACE (Farmer et al., 1999)	Argonne Nat. Lab. (USA)	Siliceous, limestone–common sand	Oxide	75–300 L	1D	Mass, composition. Induction heating. Up to 7 h 45 ablation water over melt

Recent experiments on MCCI address mainly two subjects, namely the 2D aspects of the ablation with respect to the axial versus radial erosion and the role of crust formation and melt segregation upon onset of solidification. These subjects are especially important in the analysis of the long-term erosion and cavity formation. Table 2 summarizes these tests.

One of the major findings of these tests with pure oxidic melts on 2D erosion is the observation that dry ablation tests with silica-rich concretes tend to present an anisotropic ablation pattern (more efficient ablation of the sidewalls compared to downwards ablation), whereas the tests with limestone-rich concrete show a more isotropic ablation. Anisotropic ablation has also been observed in the under-reactor room of the Chernobyl-4 reactor, where a marked lateral ablation of the (silica-rich) granitic concrete has been reported (Bogatov et al., 2007). Table 3 presents the results of the three first 2D oxidic corium–concrete interaction tests performed at ANL within the MCCI-OECD project, as an example of the observed ablation anisotropy with silica-rich concretes. A satisfactory understanding of the causes of this anisotropy is however still lacking. In the case of water flooding, COTELS tests (with siliceous concrete) indicated that water penetration in the degraded concrete walls limited sideward ablation and thus favoured downwards ablation, which continued almost at the same rate than before flooding.

3. Description of the experiments

The VULCANO facility (Cognet et al., 2000; Journeau et al., 2005) is mainly composed of an oxidic plasma-arc furnace (Jégou et al., 1998), metal induction furnaces and a concrete test section, which can be adapted to the specificity of each experiment.

A Molten Core–Concrete Interaction experimental program is underway at the VULCANO facility. It is devoted to the study of 2D long-term dry MCCI with either purely oxidic prototypic corium or with stratified oxide and metal layers (Journeau et al., 2007b). The VULCANO facility has also been used to study ex-vessel coolability by bottom flooding with the COMET concept (Journeau and Alsmeyer, 2006).

3.1. The VULCANO furnace

A furnace has been developed in order to reach melting temperatures up to 3000 °C with mixtures of various compositions [in-vessel corium (UO_2–ZrO_2, Fe), ex-vessel corium (in-vessel + concrete decomposition products: SiO_2, CaO, FeOx, Al_2O_3, MgO,...)], having a capacity of 80 kg of corium. A study of the candidate technologies resulted in choosing a transferred plasma-arc furnace (Fig. 1). Two graphite plasma torches are ignited by an electrical short circuit. The main arc is then created and transferred between these two torches, each having opposite polarity. The plasma generator gases are argon and/or nitrogen plus, in some cases, corium fumes. For our operating conditions, the maximum power is lower than 200 kW (1000 A–200 V).

The mixtures to be melted are inserted as powders in a cylindrical rotating cavity (400 mm diameter–500 mm long) and centrifugation (between 150 and 300 rpm) coats these mixtures against the furnace wall. The furnace external surfaces are water-cooled. First, a self-crucible of refractory oxides (zirconia) is achieved; then the corium powder is loaded and melted. The heating process is controlled by optical pyrometers and on-board thermocouples. There are some dissolution of the zirconia crucible and some volatilizations during the heating process so the poured composition

Table 2
Recent MCCI experiments.

Program	Lab.	Concrete	Corium	Scale (pool volume)	Geometry	Parameters
CCI (Farmer, 2007)	Argonne National Lab.	Siliceous, limestone–common sand	Uranium thermite (oxide melt)	~80 L	2D rectangular	Concrete composition. Direct current heating duration. Time of top-flooding
COMET-L (Alsmeyer et al., 2005, 2006; Sdouz et al., 2006)	FZ Karlsruhe	Siliceous	Alumino-thermite	Up to 220 L	2D cylindrical	Decay power (induction). Flooding
COTELS (Maruyama et al., 2006)	NNC Kazakhstan	Siliceous	Oxide + metal	~5 L	2D cylindrical	Induction heating. Concrete/mortar Flooding
ARTEMIS (Veteau, 2005)	CEA Grenoble	Simulant (salt eutectic)	Simulant (salts)	~12 L	1D–2D cylindrical	Gas bubbling heat flux resistor heating
MEK-T1A (Shin et al., 2002)	KAERI Korea	Basaltic	Alumino-thermite	10 L	1D	Transient test
HECLA (Sevón et al., 2007)	VTT Finland	Siliceous, EPR-type	Molten steel	~7 L	2D	Transient test

Table 3
Summary of CCI tests.

Test	CCI-1 (Farmer et al., 2004)	CCI-2 (Farmer et al., 2005)	CCI-3 (Farmer et al., 2006)
Corium load composition	61 wt.% UO_2, 25% ZrO_2, 6.4% SiO_2, 1.2% CaO, 0.4% Al_2O_3, 0.1% MgO, 5.9% Cr[a]	60.6 wt.% UO_2, 24.9% ZrO_2, 3.4% SiO_2, 3.1% CaO, 0.4% Al_2O_3, 1.1% MgO, 6.4% Cr[a]	56 wt.% UO_2, 23% ZrO_2, 11.1% SiO_2, 2.2% CaO, 0.6% Al_2O_3, 0.1% MgO, 6.4% Cr[a]
Corium mass (kg)	400	400	400
Concrete chemical composition (major constituents, after drying)	69 wt.% SiO_2 13.5% CaO 4% Al_2O_3 0.7% MgO 4.2% CO_2 3.7% H_2O	28.3 wt.% SiO_2 26% CaO 3.5% Al_2O_3 9.6% MgO 21.4% CO_2 6.1% H_2O	61 wt.% SiO_2 17% CaO 3.6% Al_2O_3 0.9% MgO 10% CO_2 3.8% H_2O
Initial temperature (K)	~2325	~2200	~2225
Test duration (before flooding) (h)	2	5	2
Ratio of horizontal to vertical ablation	Large ablation of one lateral wall	~ 1:1	~7:1

[a] Evaporated and/or oxidized in the first instants of the test.

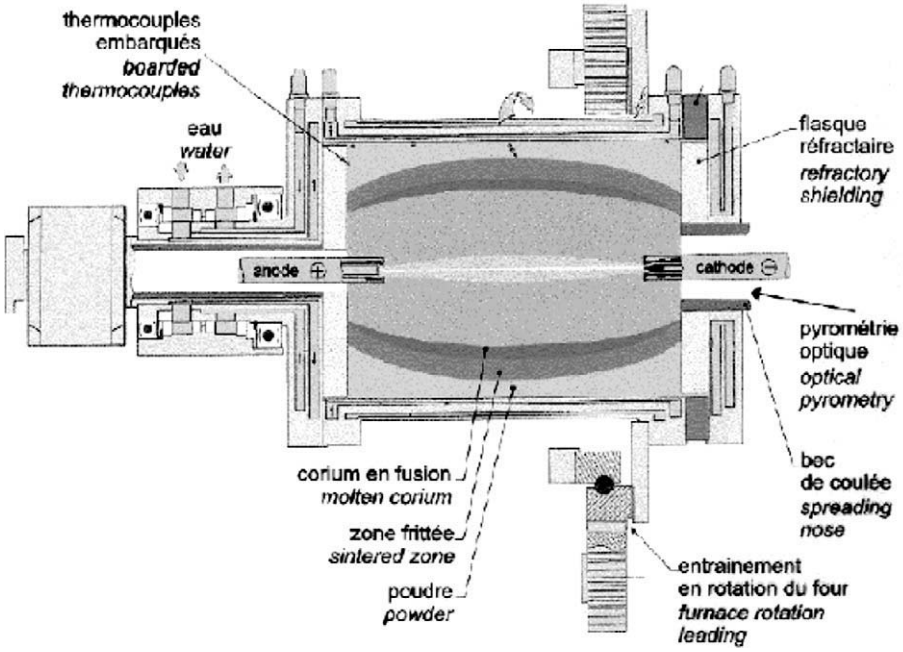

Fig. 1. The VULCANO furnace.

somewhat differs from the load composition. When a sufficient quantity of corium has been melted, the anode is withdrawn. The furnace is then tilted so that the melt pours out in the test section. The plasma-arc is maintained during the pouring operation, in order to prevent too much cooling of the melt.

3.2. Concrete test sections

The test sections (Fig. 2) are 600 × 300 × 400 mm concrete blocks with a Ø300 × 250 mm hemicylindrical cavity in which corium is poured. Two types of concretes, representative of current nuclear reactor basemats have been used. It is reminded that concrete is a complex material made of cement, water and aggregates. These aggregates are divided into sand and gravel.

Both studied concretes were made with CEM I 52.5 N cement (from Holcim) and the aggregate granulometry was the same for the two concretes (Table 4). But, the nature of the aggregates were different: In the first one (Concrete *F*), the aggregates were mostly siliceous (They came from the Rhine river – GSM Rumersheim gravel pit), while, for the second one (Concrete *G*), the sand and the gravel were a mixture of limestone–siliceous and limestone aggregates from the Durance Granulats Peyrolles ballast pit and the La Nerthe Quarry (Jean Lefebvre Méditérannée), leading to a higher fraction of limestone (Table 5). In this paper, we consider that the threshold between sand and gravel is around 6 mm. Mortar is defined as the mixture of cement, water and sand.

More than 100 K-type thermocouples (Fig. 3) have been installed in the concrete to monitor its ablation as well as some high temperature C-type thermocouples.

Four parallel induction coils surround the section and provide sustained heating (Fig. 4). The test sections are installed in the VULCANO containment and operate in air at atmospheric pressure.

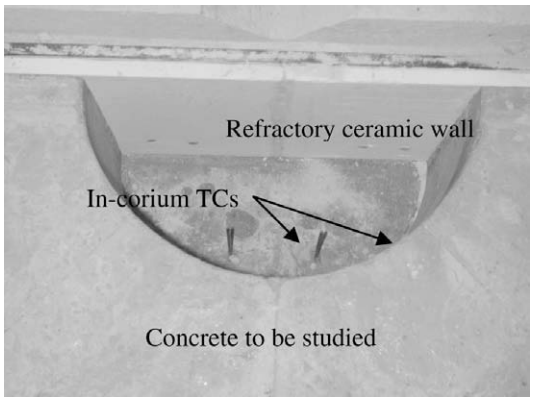

Fig. 2. The concrete crucible before corium pouring.

3.3. Description of the VB experiments

Three experiments have been performed in which a high temperature oxidic corium melt has been poured in concrete test sec-

Table 4
Weight composition used for the two concrete mixes.

Materials	wt.%
Sand 0–2 mm	12.2
Sand 0–6 mm	18.4
Gravel 5–8 mm	16.6
Gravel 8–11 mm	20.4
Gravel 11–16 mm	10.4
Cement	15.3
Water (before drying)	6.7

Table 5
Overall chemical composition of the concretes used in VULCANO MCCI experiments (wt.%).
(the total may be lower than 100% due to the minor species not reported in this table).

	Concrete *F*	Concrete *G*
SiO_2	63	26
CaO	16	42
Al_2O_3	5	2
CO_2	9	25
H_2O	3	4

Fig. 3. View of the thermocouples before pouring the concrete.

tions (Journeau et al., 2007a). Table 6 summarizes their main characteristics. Two corium load compositions and two concrete compositions have been studied.

The first corium load (VB–U4) has a solidus temperature around 1500 K and a liquidus around 2300 K, according to thermodynamic calculations with the NUCLEA database (Cheynet et al., 2004), while for the next two tests, another corium composition (including a lower fraction of concrete) was used with an estimated solidus also around 1500 K and a liquidus around 2450 K.

The three experiments followed similar procedures: the corium was molten in the furnace and poured (Fig. 5) in the crucible. Then, induction heating was turned on and maintained for at least 2 h.

Concrete ablation was monitored with consumable thermocouples inside the concrete. The concrete ablation has been tracked by the destruction of K-type thermocouples around 1200–1300 °C (Fig. 6). Temperature plateaus at 100 °C are observed, indicating the vaporization of free water. The dehydroxylation and decarbonation occurring on larger temperature ranges are not directly visible on the thermograms. High-temperature type-C (tungsten–rhenium) thermocouples embedded inside the concrete measure the corium pool temperature for a short period after the time they come in contact with the melt. Some of these sensors are installed either inside the cavity or below 1 mm of concrete for initial temperature estimation. Others are installed at deeper locations for discrete pool temperature measurements during the test.

From these thermocouples, it is possible to follow the progression of the ablation front. Fig. 7a presents the evolution of the axial and radial ablation fronts along several lines during the VB–U5 test with silica-rich concrete *F*. It clearly appears that radial ablation is on average five times faster than the axial ablation. On the contrary, for VB–U6 (Fig. 7b) the ablation rates are of the same order for both directions.

4. Material aspects of MCCI

4.1. High temperature degradation of concretes

When concrete is heated, all its components are affected. These deteriorations may be attributed to (Khoury, 2000) physicochemical changes in the cement paste (Castellote et al., 2004), in the aggregates (Campbell-Allen and Desai, 1967) and thermal expansion incompatibility between aggregates and the cement paste.

4.1.1. Differential thermal analysis

Differential thermal analysis (DTA) is a technique that measures the difference in temperature between a sample and a reference as a function of time and temperature when they are subjected to a temperature program in a controlled atmosphere (Noumouwé,

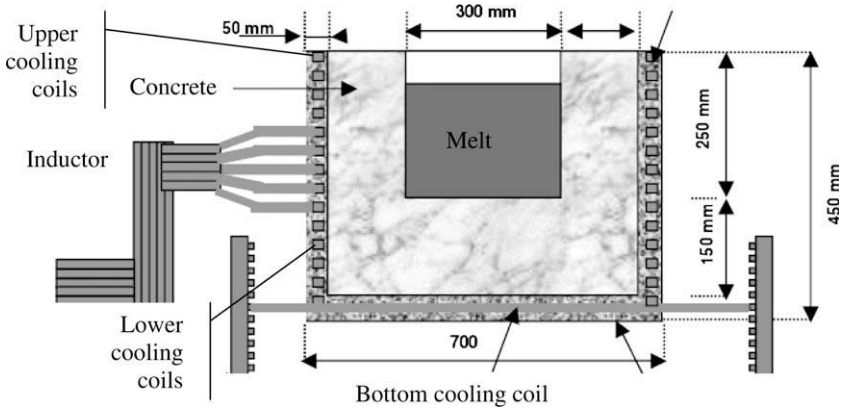

Fig. 4. Scheme of the concrete test section with induction coils.

Table 6
Characteristic of the VULCANO VB oxidic corium experiments.

Test	VB–U4	VB–U5	VB–U6
Corium load composition (wt.%)	45% UO_2, 19% ZrO_2, 20% SiO_2, 15% Fe_2O_3	69% UO_2, 17% ZrO_2, 6% SiO_2, 1% CaO, 7% Fe_2O_3	69% UO_2, 17% ZrO_2, 6% SiO_2, 1% CaO, 7% Fe_2O_3
Estimated corium pour composition (wt.%) [with partial assimilation of zirconia crucible]	40% UO_2, 43% ZrO_2, 7% SiO_2, 2% CaO, 8% Fe_2O_3	54% UO_2, 38% ZrO_2, 4% SiO_2, 1% CaO, 3% Fe_2O_3	58% UO_2, 34% ZrO_2, 5% SiO_2, 1% CaO, 2% FeO.
Corium mass	45 kg	28 kg	31 kg
Concrete	Concrete *F* silica	Concrete *F* silica	Concrete *G* limestone
Initial temperature	~2200 K	~2400 K	~2400 K
Test duration	2 h	2 h 30	2 h
Ratio of horizontal to vertical ablation	2.5:1	5:1	2:1 the first hour 1:1 the next hour

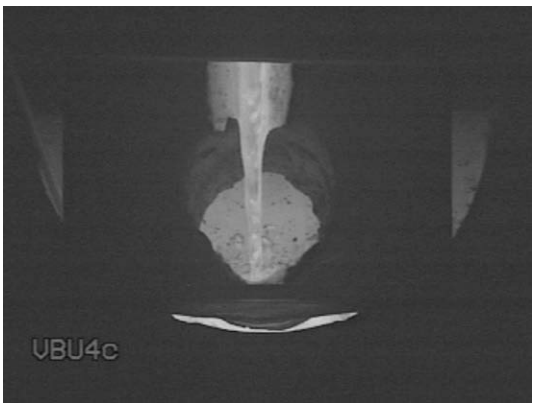

Fig. 5. Pouring of the corium in the concrete crucible.

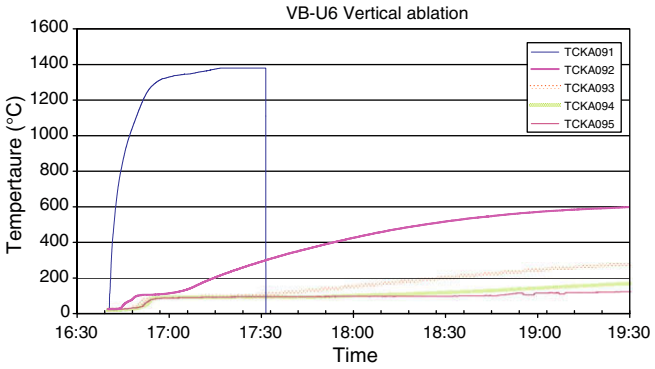

Fig. 6. Typical thermocouple readings from VB–U6 concrete.

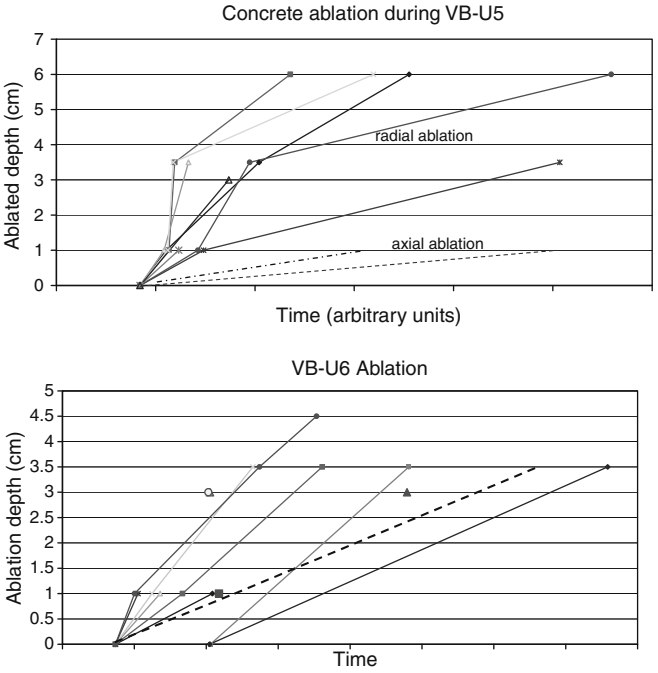

Fig. 7. Progression of the ablation front during VB–U5 and VB–U6 tests. Dashed lines represent axial ablation, solid lines represent radial ablation at various positions.

1995). It accounts for transformations by endothermic or exothermic peaks. DTA of concretes and of their constituents have been performed. Fig. 8a presents for instance the DTA of concrete *F* cement paste and gravel. It confirms that the aggregates are a mix of carbonates and of silica because of, respectively, the endothermic peak of decarbonation around 700 °C and the $\alpha-\beta$ transformation (with volume change) of quartz at 573 °C.

With regard to the cement paste, the curve highlights several endothermic peaks:

- The departures of the free and bonded water starting at 100 °C
- The stages of the calcium silicium hydroxides (CSH) decomposition starting at 150 °C
- The decomposition of $Ca(OH)_2$ into CaO and H_2O mainly between 400 and 500 °C
- The decarbonation, although this phenomenon is less dominating than in the aggregates case.

The quartz transformation is not observed, confirming the absence of crystalline silica in the cement paste.

Concrete transformations are a superposition of those of cement paste and aggregates (Fig. 8b).

4.1.2. Weight loss of concrete during heating

Thermogravimetic analysis (TGA) is used to determine the weight loss of concrete during heating. It is a technique that measures the mass variation of a sample when subjected to a temperature program in a controlled atmosphere. It is coupled with mass spectrometry to identify the nature of the released non-condensible gases. It is possible to correlate these weight losses and the transformations identified during the DTA (Fig. 8). The weight loss of concrete is due to many phenomena (Fig. 9): release of H_2O (3 ± 1 wt.%) due to the loss of free water (~100 °C), the loss of bonded water, the decomposition of $Ca(OH)_2$ (400–500 °C) and the loss of CO_2 (10 ± 0.2 wt.%) at around 700 °C.

The water losses come from the cement paste whereas the release of CO_2 is mainly due to the limestone in the aggregates.

4.1.3. Microcracking induced by heating of concrete

Microcracking is one of the consequences of the damages due to heating (Georgali and Tsakiridis, 2005). The loss of water which induced the transformation of hydrated products and the volume changes (aggregates and cement matrix) during heating are responsible for most of the microcracks which appeared into the concrete. The cracking of the concrete exposed to high temperatures has many causes: different coefficient of thermal expansion between aggregates and the cement paste; presence of an initial microcracking in the cement paste; microcracks into the cement matrix and around aggregates expand from 300 °C; cracks preferably grow into the cement paste and also in the aggregates and become visible to the naked eye.

The formation of microcracks is visible at exposure temperatures above 300 °C; they initiate inside the cement paste. At higher temperatures, above 500–600 °C, aggregates are also deteriorated and microcracks extend around and into them. Fig. 10 presents as examples photographs of concrete samples exposed to 600 °C (presenting microcracks less than 1 cm long) and to 800 °C (This sample has lost most of its mechanical strength and exhibits long wide cracks).

4.2. Post Test Examinations of VB experiments

In VULCANO experiments, Post Test Analyses are an important tool to understand the processes that occurred during the test (Journeau et al., 2001), in conjunction with the online measurements. After the end of the test, the test sections are dismounted and observed (Figs. 11 and 12). The shape of the remaining concrete is measured by laser telemetry and samples are collected

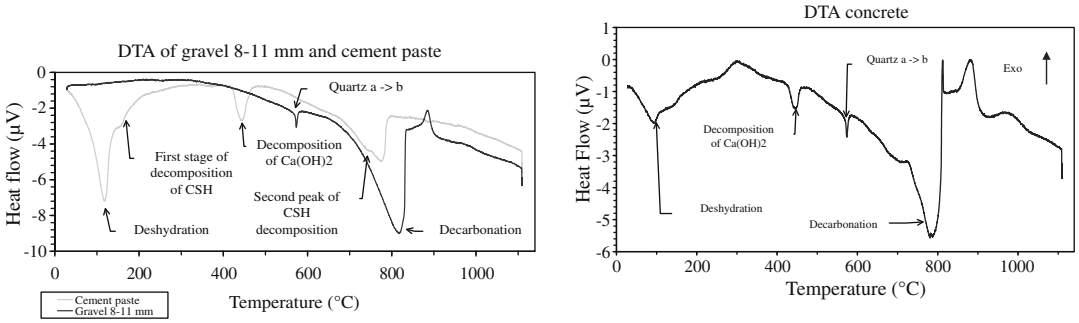

Fig. 8. (a) DTA of gravel 8–11 mm and cement paste and (b) concrete *F*.

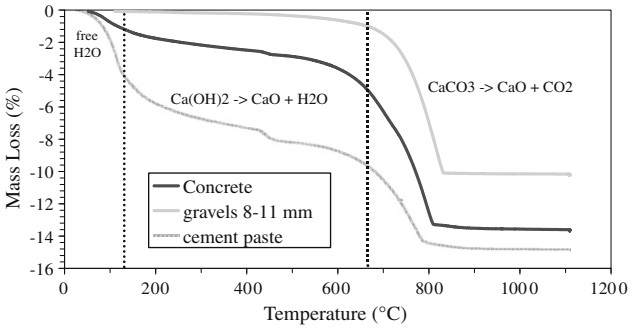

Fig. 9. Thermogravimetric analysis of concrete *F*.

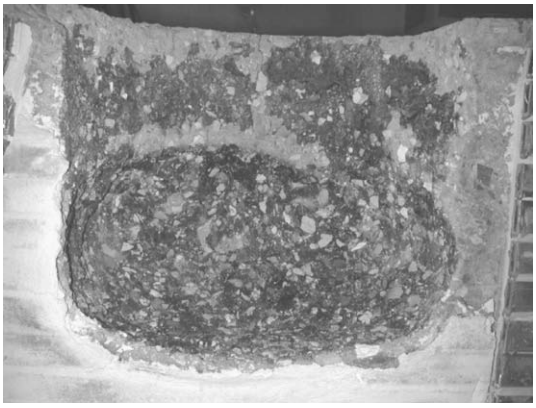

Fig. 11. Post-test view of the concrete cavities for VB–U5 (silica-rich concrete *F*).

Fig. 12. Post-test view of the concrete cavities for VB–U6 (limestone-rich concrete *G*).

for analysis. The concrete ablation anisotropy for the siliceous concrete was confirmed by these analyses.

In the tests with siliceous concrete, unmelted siliceous aggregates have been observed inside the corium (Fig. 13). For the limestone-rich concrete, it is possible to observe decarbonated limestone (in white on Fig. 12) in the ablated concrete block.

The collected samples were observed using a Stereoscan CAMBRIDGE S360 scanning electron microscope (SEM) in the backscattered electron mode, in order to obtain a contrast connected to the chemical composition of the phases which are seen (the higher the mean atomic number, the brighter the phase in the micrograph). Moreover, phase compositions were measured by means of Energy Dispersive Spectrometry microanalysis (Oxford ISIS 300).

In the two tests with silica-rich concrete, SEM micrographs of corium near the interface showed the presence of horizontal zones of different compositions. They include molten mortar (with few percents of corium), concrete-rich corium–concrete mixtures and finally the pool corium–concrete mixture. Fig. 14 presents the microstructure of concrete below this interface in a VB–U5 sample. Three zones are visible: on the top, an interaction zone in which

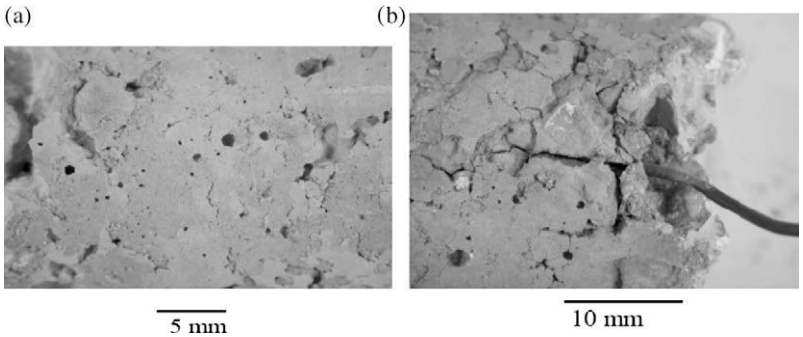

Fig. 10. Macrographs of concrete *F* samples subjected to (a) 600 °C and (b) 800 °C.

Fig. 13. Corium sample including unmelted siliceous aggregates.

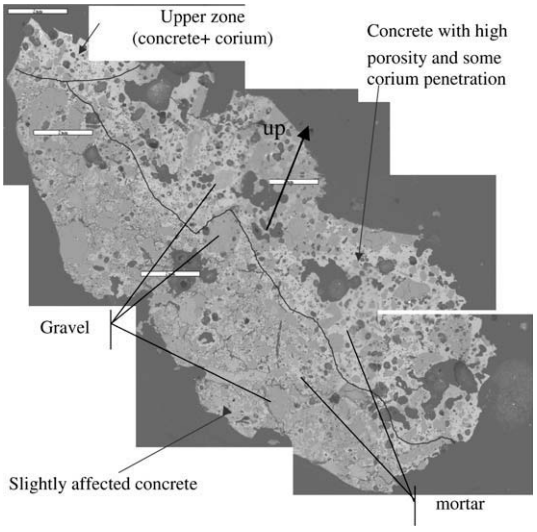

Fig. 14. Composite micrograph of the concrete near the lower corium–concrete interface. For VB–U5 with silica-rich concrete *F*.

some corium has been mixed with molten mortar. Then a zone is visible in which a large porosity (~20%) is observed. There are some small inclusions of corium, which formed uranium and zirconium silicates. Finally, the last zone is less affected and shows individual aggregates rich either in silica or in calcia. Plumes and droplets of mortar-rich composition have been observed in both tests with silica-rich concrete *F*.

Fig. 15 presents the compositions obtained for 24 VB–U5 analysis windows with EDS. These windows have been taken inside the corium pool, in the interaction zones (both at the bottom and the sides of the pool) and in the slightly affected concrete (near the interface). It appears clearly that all these compositions are almost aligned and correspond to mixtures, at various proportions, of $(U,Zr)O_2$ with mortar (cement paste + sand) instead of concrete (cement paste + sand + gravel). It must be noted that the difference between these two end-compositions is larger than the analysis uncertainties.

A similar observation was done in the VB–U4 test samples (also with concrete *F*). Due to the difference in melt pool temperature between these two tests, it is unlikely that evaporation of silicon-containing vapors (e.g. SiO) can explain the loss of silicon compared to a postulated corium–concrete mixing. This indicates likely

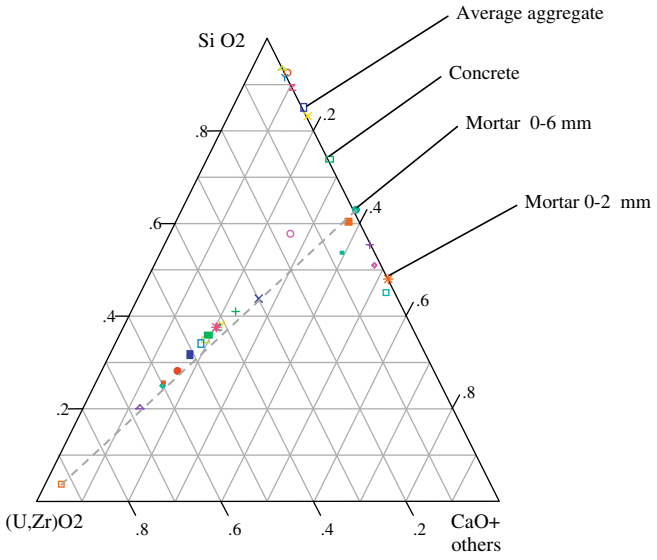

Fig. 15. Ternary plot presenting the mass composition obtained by EDS from all the analysed windows in VB–U5 samples.

that the gravel did not mix with corium at any of the analysed locations.

Maruyama et al. (2006) who reported COTELS prototypic corium tests in identical conditions with concrete and mortar indicated that "the ablation rate for basaltic [siliceous] concrete was significantly smaller with one for mortar" and that "a layer of the degraded concrete including coarse and fine aggregates were formed", confirming our observations.

In the case of the test VB–U6 with limestone-rich concrete *G*, no horizontal layering was identified, contrary to what was found in the other two tests with silica-rich concrete *F*. Two zones of different composition have been observed which can be interpreted as a plume of ascending concrete-rich liquid in corium (Fig. 16). A similar feature had been observed on a sample from the CCI-2 experiment (Farmer et al., 2005) performed with an US

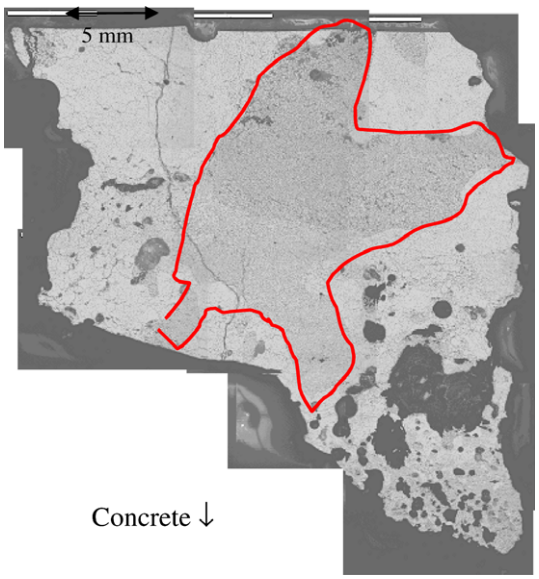

Fig. 16. Composite micrograph of the VB–U6 corium near the lower limestone-rich concrete interface (the concrete-rich plume is within the red curve). (For interpretation of the references to colour in this figure legend, the reader is referred to the web version of this article.)

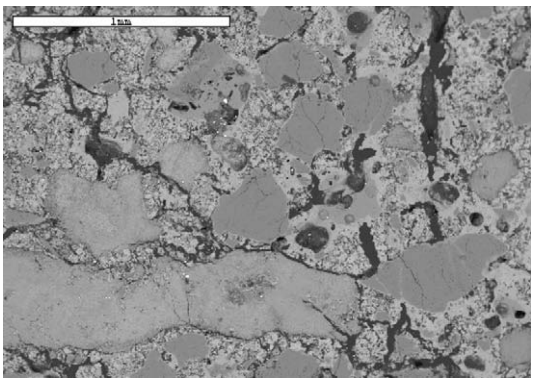

Fig. 17. Corium nodules found inside partly molten mortar below the lower corium–concrete interface.

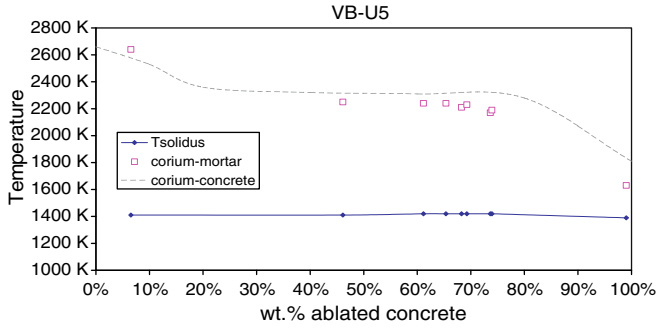

Fig. 18. Pseudo-binary corium–mortar phase diagram (each square corresponds to an experimental composition).

limestone–common sand concrete. The concrete near the interface had lost all mechanical strength, preventing an effective sampling of the concrete side.

One sample from VB–U6 has been analysed successively in three European material analysis laboratories and this round robin exercise (Bakardjieva et al., 2008) concluded that the uncertainties in the elemental composition obtained from SEM/EDS was of about 1/10th of the measured value, except for light elements such as oxygen where the discrepancy was around 1/4th .

The VB–U6 EDS compositions were also found to be rather aligned on a ternary plot, showing a mixing of the corium with the composition of the concrete, which for corium *G* almost equals that of the mortar. So, it is here impossible to determine if gravel was mixed or not with corium. Due to the decarbonation, remaining carbonate gravel was indeed transformed into powder before the concrete solidus temperature and must have behaved as sand particles.

4.3. Spatial distribution of the measured compositions

Different compositions have been observed in the VULCANO VB–U samples. No difference in local melt composition has been found between the lower and lateral interfaces, even in the VB–U4 and VB–U5 tests for which a large ablation anisotropy has been observed.

The major trend, observed for both types of concretes and both interface orientations, is that there are definite zones (layers, plumes) with rather homogeneous compositions rather than a gradient of composition. This shows that the compositional mixing is due to convection rather than diffusion. Compositional convection seems to come mainly from plumes. The other mode of mixing of mortar/concrete-rich and corium-rich mixtures is thanks to the transport of droplets of mortar/concrete-rich material. These bubbles range usually from 100 μm to 2 mm and have been found in all samples. There are also mortar-rich films around the gas bubbles. There seems thus to be two modes of solutal convection, with plumes and with drops. The absence/presence of convective plumes near an interface is clearly related to the convective heat and mass transfer.

5. Modeling

Several models of Molten Core–Concrete Interaction have been developed leading in particular to the CORCON (Bradley et al., 1993), WECHSL (Foit, 1997), CORQUENCH (Farmer and Spencer, 1999), MEDICIS (Cranga et al., 2005), COSACO (Nie, 2005) and TOLBIAC-ICB (Spindler et al., 2005) computer codes. In the earlier codes, the chemical thermodynamic aspects of corium–concrete interaction were decoupled from the mainly thermal ablation, while strong coupling is considered in the latest codes.

5.1. Analysis with TOLBIAC-ICB

TOLBIAC-ICB (Spindler et al., 2005) assumes that the convecting pool interface temperature is set to the pool liquidus temperature, according to the phase segregation model (Seiler and Froment, 2000). The main hypotheses are that a solid crust deposits at the concrete walls and the pool is only composed of liquids and has thus a low viscosity. The crust thickness is estimated using a thermal steady-state model and local thermodynamic equilibrium is assumed at the crust–pool interface.

The three VULCANO corium–concrete interaction tests have been computed with the TOLBIAC-ICB computer code. Since there is currently no model predicting the ablation anisotropy, the ratio of the lateral heat flux to the vertical one is a user input. Once this data is provided, from Post Test Observations, the code is able to follow the concrete ablation progression.

For instance, Fig. 19 presents the computed ablation rates for the test VB–U5 with silica-rich concrete. The comparison with the ablation front progression measured by thermocouples leads to a good agreement. The concrete cavity shape evolution is also well calculate by this model. Fig. 20 compares, for the test VB–U6 with limestone-rich concrete, the experimental and calculated shapes. The main uncertainty in following the cavity shape is due to the fact that type-K thermocouples are destroyed at a temperature lower than the "concrete melting temperature" (as defined by the code developers) for this limestone-rich concrete.

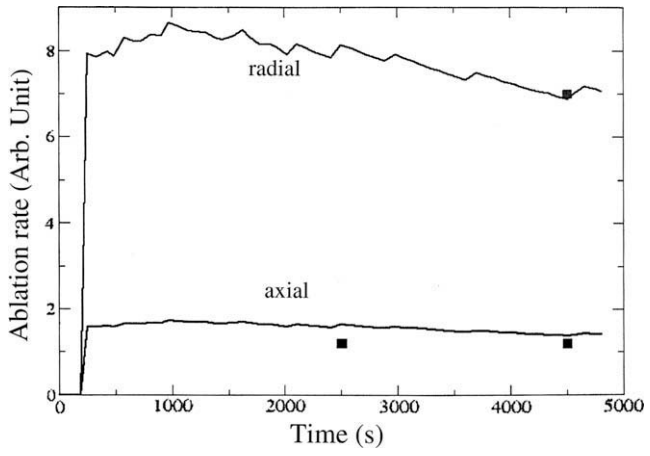

Fig. 19. Axial and radial ablation rates (VB–U5) lines: TOLBIAC-ICB calculations – squares: experiment.

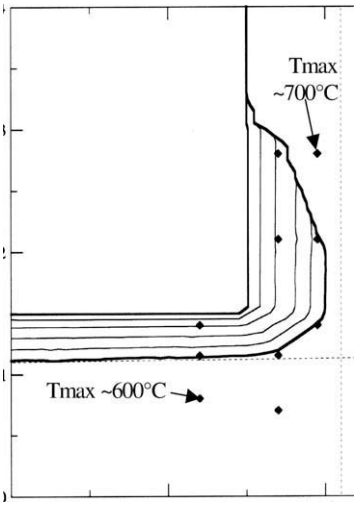

Fig. 20. Progression of the concrete ablation for test VB–U6. The dots indicate the thermocouple positions (at 90°). The dashed lines indicate the zone where no thermocouple reached 1200 °C.

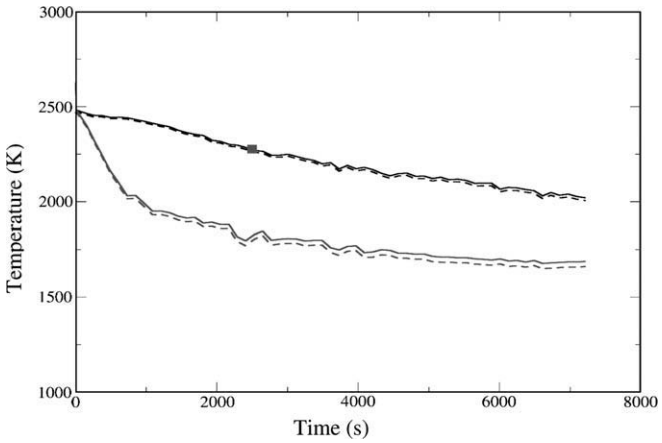

Fig. 21. TOLBIAC-ICB Calculations of VB–U6 melt pool temperature for the two solidification hypotheses lines: estimated melt pool temperature – dashes: estimated melt pool liquidus temperature – square: measured pool temperature upper (black) curves: homogeneous solidification hypothesis – lower (grey) curves: phase segregation hypothesis.

TOLBIAC-ICB computes the crust thicknesses from the heat fluxes at the various interfaces. For VB–U5, the upper surface and lateral wall crust thicknesses tends to 1 cm, the inert refractory wall crusts grow up to 1 cm and are then dissolved, while the lower crust increases up to 6 cm. For VB–U6, the crusts deposited on concrete (both at the bottom and sides, due to the isotropy) reach 2 cm. A crust deposition characteristic time can be defined as the time necessary for the heat flux to extract the latent heat related to the equilibrium crust thickness (Seiler and Froment, 2000). Since, the crust thickness t can be related to the conductive heat flux at equilibrium F by:

$$h = \frac{k(T_{\text{liquidus,corium}} - T_{\text{"melting",concrete}})}{F} \tag{2}$$

It occurs that the characteristic crust solidification time, corresponds to the time when a quantity of heat $Q = \rho \cdot H \cdot h$ is extracted from a unit interface area. Thus,

$$\tau = \frac{k \cdot \rho_{\text{corium}} H \Delta T}{F^2} \tag{3}$$

For the test VB–U6 with isotropic ablation of the limestone rich concrete, the characteristic time is of 700 s, much shorter than the 2 h of test. For the lateral crusts in VB–U4 and VB–U5, this time ranges between 500 and 1100 s, which is similarly small compared to the test duration. On the contrary, due to low heat fluxes at the lower silica concrete interface, the characteristic times for the lower crust growth are of 7000 and 12,000 s, respectively, actually longer than the test duration. Due to the observed low heat fluxes at the lower surfaces, much longer experiments should be advised for silica-rich experiments. This would lead to large lateral ablations that can exceed the capabilities of our test section, which had been implicitly designed for isotropic ablation.

Let us focus now on the chemical nature of the deposited crust. There are two possible hypotheses: either, at each time step, the deposited crust is at the solidus composition, which is richer in refractory species (mainly UO_2 and ZrO_2) than the melt, or the crust has the same composition as the melt pool. The relatively small volume to surface ratio of the VULCANO test section implies that these two hypotheses will lead to very distinct results. Fig. 21 shows that, in the case of segregation, the pool being depleted in refractory material, its liquidus temperature will fall significantly, and, as it follows the liquidus temperature, the pool temperature is computed to be, after 2000 s, 500 K lower than with the homogeneous crust hypothesis. In all the three experiments, the pool temperature measurements (obtained when a type-C thermocouple installed in the concrete was uncovered by ablation) confirm the homogeneous crust hypothesis. This is also supported by the fact that no refractory crust has been found during the Post Test Examinations. This result is consistent with previous researches (Journeau et al., 2003a) showing that planar or cellular solidification – which cause macrosegregation – cannot happen when there is a significant fraction of silica in the melt, due to a too small mass diffusion coefficient. This threshold between macrosegragation and homogeneous crusts was established from tests without bubbling around 25 mol% silica (Frolov, 2004).

5.2. Transient modeling with CRUST

To assess the transient phase of the interaction, the transient conduction code CRUST has been used. This code (Gatt et al., 1995; Journeau et al., 1999) models one-dimensional transient behaviour of a corium–substratum multilayer system, taking into account the phase change but considering only thermal conduction and thermal radiation. An enthalpic formulation is explicitly solved allowing for sub-mesh determination of the phase change front. Volume heat generation is taken into account in the corium layer.

The whole pool is modeled with radiation on the top surface and convection can be roughly taken into account thanks to a multiplicative factor applied to conduction. The decay heat is simulated in order to generate the experimentally found long-term average heat flow. Fig. 22 compares the CRUST calculations at the depths of 4 type-K thermocouples embedded in the concrete below the pool for test VB–U6. These thermocouples have been chosen far away from the inert wall to avoid 3D effects. Due to the uncertainty on the precise position of the sensors, a sensitivity analysis has been performed and the best results (max. discrepancy of 32 K after 1800 s) were found with depth modified by less than 0.2 mm. Similarly good fits have been obtained for tests VB–U4 and VB–U5.

Type-C thermocouples positioned slightly below the initial concrete surface provide some insights to the interface temperature. Using a thermal contact resistance of 1.7×10^{-3} K m^2/W enables to recalculate the interface temperature with CRUST, leading to an average discrepancy of 40 K (Fig. 23). The remaining discrepancies may be attributed to the temporal variations at the interface between a solidifying pool and a wall (Loulou et al., 1999). It must

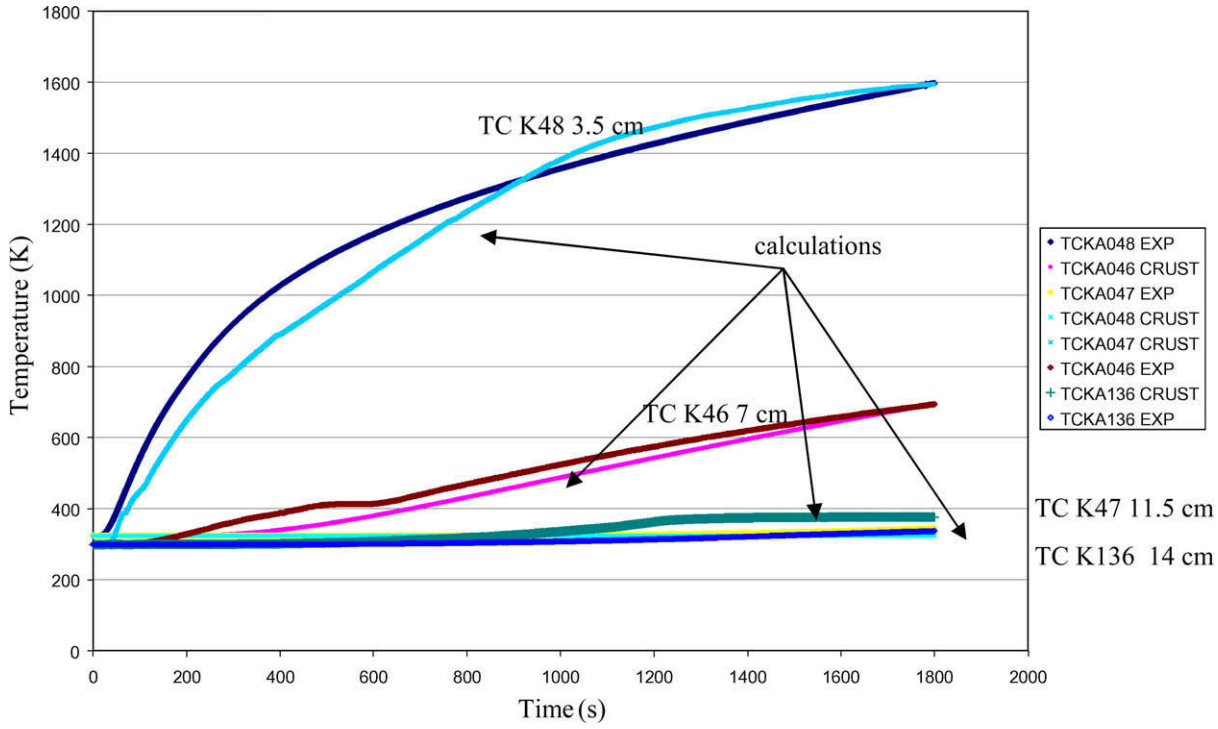

Fig. 22. Measured and calculated temperature transients at several depths in the concrete below VB–U6 corium pool.

be noted that all three tests may be fairly reproduced with thermal contact resistances between 1 and 4×10^{-3} K m^2/W. This falls within the range of thermal contact resistances that had been experimentally found during the VULCANO spreading tests over ceramic or concrete substrates (Journeau et al., 2003b).

These calculations show that, as soon as there is a good estimation of the heat flow to each surface, current models are able to provide a good estimation of the experimental data. The remaining effort on oxidic MCCI modeling should aim at predicting the repartition of the heat flow between the vertical and horizontal surfaces.

5.3. Analytical models

In order to provide some more insight to the heat and mass transfer occurring during the corium–concrete interaction, an analytical model has been proposed (Carénini et al., 2007).

When hot corium is poured over cold concrete, the thermal shock leads to the formation of a crust at the interface, which will grow up and eventually remelt, due to the heat transferred from the corium pool which is subject to radioactive decay heat. This is modeled by quasi steady states. The geometry and the notations are presented in Fig. 24.

The crust growth characteristic time is evaluated by equating the heat flux F_a coming from the corium pool, the heat flux needed to cool and solidify the crust and the steady-state conduction heat flux through the crust:

$$\tau_c = \frac{\rho_0\{H_0 + c_p(T_0 - T_{liq})\}k_c(T_{liq} - T_{cm})}{F_a^2} \quad (4)$$

A system of six equations with six unknowns (the thicknesses of the crust h_c, the molten concrete h_m and of the effectively heated solid concrete h_s, the heat flux F across the layers, the interface temperature T_{cm} and the crust characteristic time τ_c) and can be resolved

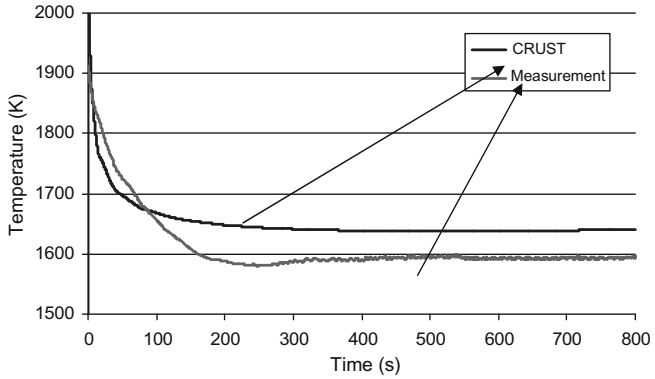

Fig. 23. VB–U4 interface temperature (measured by a type-C thermocouple) and calculated by CRUST.

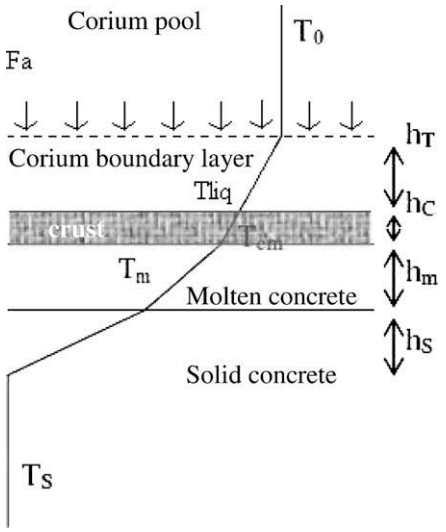

Fig. 24. Corium–concrete lower interface with crust.

numerically (Carénini et al., 2007). The main results of an application to the VULCANO VB tests, assuming that solutal convection is the main cause of convective heat transfer, are shown in Table 7. It must be noted that both tests present similar characteristics, with a slightly larger crust for the test with silica-rich concrete.

As a consequence of decay heat, crust continues being heated. Once the maximum crust thickness is reached, it will begin to remelt. A new set of four equations with four unknowns (molten crust thickness h_{c1}, molten concrete layer thickness h_{m1}, heat flux F and the interface temperature T_{cm1} between crust and melt) can be resolved numerically (Carénini et al., 2007). Table 8 presents the melting that has been done in 1 h after the maximum thickness has been reached. The melting rates are of the same magnitude for both tests, but as the maximum crust thickness was lower above the limestone-rich concrete, the crust is thinner after 1 h. The major difference is with the crust lower face temperature, which is 300 K higher in VB–U6 than VB–U5, whereas the difference was twice smaller at the time of maximum crust thickness. In both cases, the molten concrete thickness is of about 2 cm at this time.

The effect of convective dissolution of corium crust by molten concrete has also been studied. It must be noted that molten corium is denser than molten concrete, so dissolution of denser corium will favor convection (Fig. 25). Moreover, as shown by the corium–concrete pseudobinary phase diagrams (Figs. 27 and 28), mixing corium with some concrete results in a lower liquidus temperature, enabling a dissolution process.

Using Kerr (1994a) model of convective dissolution, the dissolution rate can be expressed as:

$$V_i = \frac{(1-C_i)^{4/3}}{C_i}\left(\frac{g(\rho_0-\rho_m)D^2}{\mathrm{Ra}_c\mu_m}\right)^{1/3} \quad (5)$$

assuming that the crust is made of pure corium over a melt of pure concrete, with a critical Rayleigh number Ra_c of $(0.32 \pm 0.04)^{-3}$ (Kerr, 1994a). Applying Mungall (2002) empirical model of chemical diffusion in silicate melts, as recommended by Frolov (2004), diffusion coefficient in molten concrete for U^{4+} ions are estimated at the order of 10^{-11} m^2/s and of 10^{-10} m^2/s, respectively, for VB–U5 and VB–U6 at the concrete melting temperature. The evolution of the dissolution rate is plotted on Fig. 26 for both tests. On both plot, the temperature axes range from the initial contact temperature to the corium liquidus temperature. The crust lower face temperature will move between these two temperatures during the solidification and melting/dissolution phases. At temperatures below the corium–concrete liquidus curve, dissolution will not be efficient. Then, above liquidus (2000 K for VB–U5 and 2100 K for VB–U6), the dissolution rates increase almost exponentially with temperature.

For the case with limestone-rich concrete, large dissolution rates (between 2 and 12 cm/s) have been found, whereas it is limited to 3 cm/s for the VB–U5 case. Therefore, with limestone-rich concrete, the crust will be dissolved more rapidly and the crust will be destructed both by melting at the upper surface and dissolution at the lower surface. This will be amplified by the fact that for the limestone-rich concrete, the crust lower face temperature is computed to be higher than for silica-rich concretes.

Moreover the total time for crust formation and disappearance is of the order of 1 h with VB–U6, which corresponds to the time for which in this test, anisotropic ablation was observed. For VB–U5, the lower crust would be present for about 4 h (i.e. more than the test duration).

One of the possible interpretations of the differences between silica-rich and limestone-rich concretes regarding their interaction with corium is that the interfaces facing the corium pool would be different for those two types of concrete.

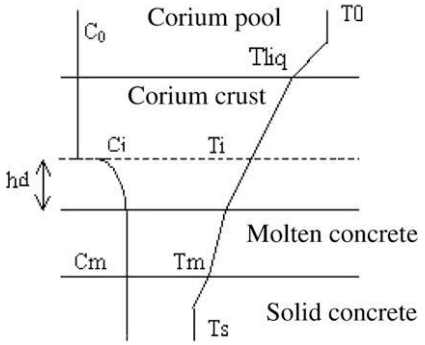

Fig. 25. Dissolution of corium crust by molten concrete on the left-side curve: concentration of concrete, on the right-side curve: temperatures.

Table 7
Crust formation characteristics.

Test	VB–U5	VB–U6
Solidification time τ_c	2210 s	1330 s
Solidification rate V_m	1.8 cm/h	1.7 cm/h
Maximum crust thickness $h_{c,max}$	6.6 cm	4.8 cm
Crust lower face temperature T_{cm}	1736 K	1893 K

Table 8
Crust melting characteristics 1 h after maximum.

Test	VB–U5	VB–U6
Time τ_c + 1 h	5810 s	5130 s
Crust thickness h_c	4 cm	2 cm
Melting rate V_m	1.7 cm/h	2 cm/h
Crust lower face temperature T_{cm}	1920 K	2220 K

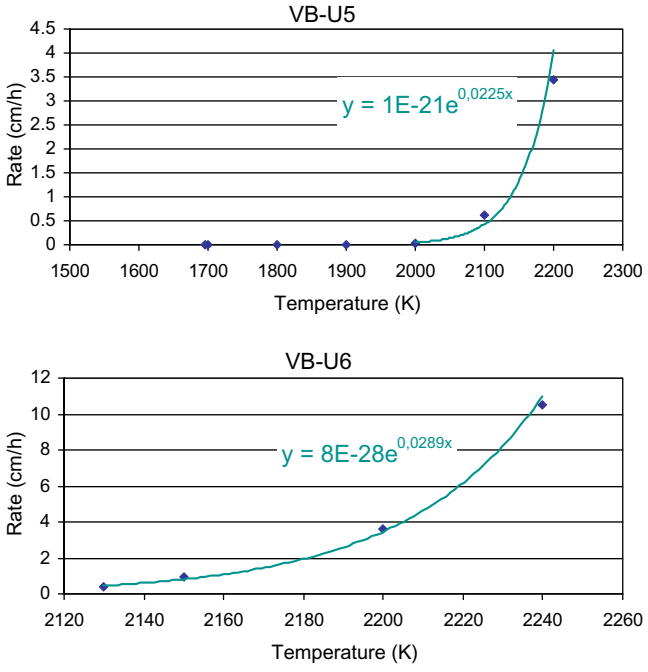

Fig. 26. Evolution of dissolution rates with temperature for VB–U5 and VB–U6. Both plots are between initial and liquidus temperature.

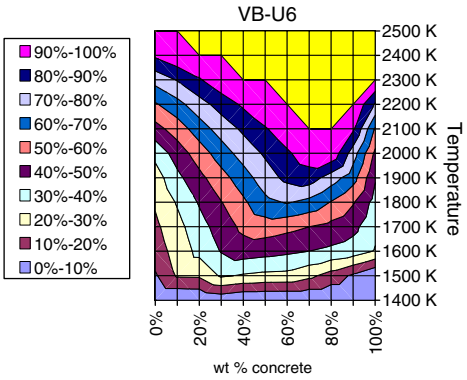

Fig. 27. Pseudobinary corium–concrete phase diagrams for limestone-rich concretes (VB–U6. 0% corresponds to the corium load compositions (including concrete decomposition products).

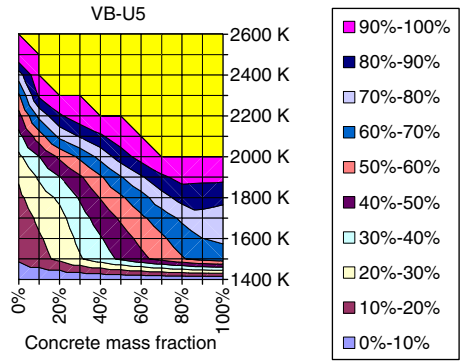

Fig. 28. Pseudobinary corium–concrete phase diagrams for siliceous concrete (VB–U5). 0% corresponds to the corium load compositions (including concrete decomposition products).

For limestone-rich concretes, the crust will not be stable on all the interfaces, due to mechanical instability in the sidewalls and remelting and dissolution by molten concrete in the bottom surface. Then, after an initial transient, of the order of 1 h, the heat exchanges as well as the ablation profiles will be isotropic.

In contrast, silica-rich concrete will favor the presence of more stable crusts at the bottom due to the much smaller dissolution and to the increased thickness caused by corium cooling by colder silica gravels. Stable crusts will only be found on the bottom interface while the crusts on the sidewalls will be subject to mechanical instabilities. These anisotropic boundary conditions for the corium pool will lead to anisotropic heat transfers and ablation profiles.

This preliminary modeling has been validated on the VULCANO MCCI tests. It provides a possible explanation of the observed ablation anisotropies. A corium pool thermalhydraulic model taking into account different interface temperatures depending on the stability of horizontal and vertical interfaces has still to be developed in order to achieve quantitative predictions of two-dimensional Molten Core–Concrete Interactions. The effect of sparging gas must also be introduced in an explicit manner in this model before it could be included in a MCCI code.

5.4. Consequence of the absence of silica gravel in the pool

The VB–U4 and VB–U5 Post Test Examinations indicate that, for the silica-rich concrete *F*, siliceous gravel did not mix with the corium pool. Nevertheless, since about 11.6 kg of concrete has been ablated in VB–U4, about 5–6 kg of gravel should be found. The observed gravel does not account to the whole inventory. According to calculations using GEMINI2 and the NUCLEA061 database (Cheynet et al., 2004), heating a 50 wt.% mortar–50% silica mixture gives two liquids, one being almost pure SiO_2. It is thus possible that molten silica forms droplets that will float towards the surface, being lighter than the corium–mortar mixture. A 2 cm layer would correspond to the 5–6 kg of ablated gravel. This area was unfortunately not sampled during the Post Test Examinations, which were at the time focussed on the corium–concrete interfaces. It is now impossible to verify this hypothesis on the remains of these tests since the corium pool has been broken into pieces during the dismounting and sampling process and its geometry has been lost, preventing the selection of surface samples. Thermodynamic calculations with GEMINI2 and the NUCLEA database indicate that the mortar *F* solidus temperature is around 1150 °C, close to that of the concrete *F*. On the opposite, its liquidus is at 1390 °C compared to 1700 °C for the complete concrete mix, while crystalline silica (cristobalite) melts at 1726 °C (Wriedt, 1990). Moreover, mortar is 50% liquid (and thus may effectively flow) just above the solidus temperature, while this fraction is only achieved around 1380 °C for the melting concrete.

It can be seen from Table 4 that 1 ton of concrete (approximately 0.5 m^3) contains 460 kg of mortar and 474 kg of gravel, i.e. almost the same masses. So, the corium pool will be about twice less rapidly diluted by light oxides than in the theoretical case of a mixing of the corium with all the ablated concrete (See Fig. 17).

A pseudo-phase diagram (Fig. 18) has been drawn by considering for each given fraction of ablated concrete, the mass of mortar which effectively mixed with corium. It appears that the liquidus temperature is close to that obtained for the theoretical mixing of corium with all concrete. This is caused by a counterbalance between the effect of a lower fraction of light oxides (when only mortar is mixed to corium) and the fact that mortar is more fusible than concrete.

The amounts of heat necessary to melt concrete, mortar and gravel and bring them to the pool temperature are of the same order of magnitude (Table 9) this should not affect drastically the heat exchanges due to the ablation. Corium mixing only with mortar will also affect the melt properties and in particular its viscosity. Table 10 presents the viscosities estimated with Ramacciotti et al. (2001) methodology at 2300 K (concrete *G* liquidus temperature) for various compositions. Whereas, for the limestone-rich composition *G*, mortar and concrete have roughly the same composition and thus have similar viscosities. Mortar F viscosity is about four times larger than that of mortar *G* (a similar four times increase is caused by a temperature decrease of 250 K), while molten concrete *F* viscosity is 75 times larger. Thus, although there is a huge difference in viscosity between both molten concretes, this is not the case for the molten mortars, and will be even less the case for corium–mortar mixtures. Therefore, it is unlikely that differences in molten mortar viscosity cause the observed differences in ablation behaviour except in case of a cliff-edge effect between 30 and 125 mPa s (1 and 5×10^{-5} m^2/s).

In summary, even if the pool composition evolves differently if gravel do not mix with corium in the siliceous-rich concrete exper-

Table 9
Enthalpy needed to heat and melt mortar *F*, quartz aggregate and concrete *F*.

	Mortar *F*	Quartz	Concrete *F*
From 298 K to 1430 K (solidus)	1.6 MJ/kg		
From 298 to 1660 K (mortar liquidus)	2.4 MJ/kg		
From 298 K to 2000 K (silica melting point)	2.9 MJ/kg	2.1 MJ/kg	2.4 MJ/kg

Table 10
Estimated viscosities at 2300 K for the VULCANO concrete and mortar compositions.

	Concrete *F*	Mortar *F*	Concrete *G*	Mortar *G*
Estimated viscosity (MPa s)	2300	125	28	31

iments, it is unlikely that this is the direct cause of the observed anisotropy.

Another effect is that the observed floating silica gravel at the boundaries of the corium pool (Fig. 13) can serve as cold spots and will enhance crust formation (see Appendix A).

If it is assumed that there is a second silica-rich liquid (due to the miscibility gap in molten concrete *F* at intermediate temperatures and/or to the separate melting of mortar and of silica gravel), the presence of this liquid may definitely affect the convective flow pattern between silica-rich concretes (with two immiscible liquids, one being very viscous – the viscosity of silica (Urbain et al., 1982) at 2300 K is of the order of 10^7 mPa s, the other being molten mortar *F*) and limestone-rich concretes.

Theses two last effects may contribute to the different ablation shapes observed between silica-rich and limestone-rich concretes but further research is required to model these effects and assess their possible contribution to anisotropy.

5.5. Transpositions to reactor case

The 2D experiments show that silica-rich concretes (VB–U4, VB–U5, CCI-1 and CCI-3) are ablated by corium in a different way than limestone-rich concretes (VB–U6, CCI-2): anisotropic with a preferential ablation of sidewalls for the former, more or less isotropic for the latter (except the initial transient in VB–U6). Up to now analysis of those tests did not enable us to determine which phenomenon was causing this change of ablation pattern. Therefore, it is quite difficult to transpose these results to reactor scale without a validated predictive model.

Nevertheless, it is assumed that the observed anisotropy with silica-rich concretes is not an artifact due to experimental set-up or small scale. Under the EU-funded CHESS project, Kurchatov Institute has mapped the layout of corium in Chernobyl-4 reactor room (Bogatov et al., 2007) showing that there has been a large-scale anisotropic corium–concrete interaction with basaltic concrete.

Some results have anyhow been already gained that can help us differentiate between different models: The pool temperature evolution is compatible with models in which it is closer to the pool liquidus temperature than to the solidus temperature – e.g. Cranga et al. (2008) best fitted the interface between 0.6 T_{liq} + 0.4 T_{sol} and 0.9 T_{liq} + 0.1 T_{sol} for the CCI-2, CCI-3, VB–U5 and VB–U6 tests. The assumption that there are no macrosegregated crusts, i.e. that the crust and the pool have the same composition has been validated on VULCANO tests with TOLBIAC-ICB calculations and confirmed by Post Test Examinations which have not shown any segregated crust.

The main other finding is related to the fact that the siliceous gravel did not mix with the corium pool. In the reactor cases, where two liquid phases coexist – an oxide and a metal (mostly molten steel) – the fact that only half the mass of light species mixes with corium implies that approximately twice more ablation will be required to reach the point where the oxide becomes significantly lighter than metal. So stratification will occur later than expected with the assumption of perfect mixing between concrete and oxidic corium.

6. Role of the concrete nature

6.1. Evaluation of the differences between silica-rich and limestone-rich concretes

Further knowledge is needed to determine and model the causes of the observed differences in ablation shape between the two types of concretes we studied. The difference between these two kinds of concrete (Journeau et al., 2008) are listed hereunder in order to try to identify most of the parameters that can play a role on the concrete ablation shape through either MCCI thermal–hydraulic (gas release, pool viscosity, intermediate layer at interface, void fraction value and heat exchange surface...) or interface condition (mixing process between concrete and corium, crust formation and crust stability, concrete decomposition...).

6.1.1. Gas release

Limestone (calcium carbonate)-rich concretes generate more gas on heating than siliceous concrete, thanks to $CaCO_3$ decarbonation. Twice as much gas is, for instance, generated, at constant ablation rate, by the VB–U6 concrete than by VB–U5 concrete. Since the limestone-rich concrete requires a higher enthalpy to be molten, this ratio is somewhat lower (~1.5:1) at constant heat flux.

The change in the gas flow rate during MCCI could affect:

- Crust mechanical stability at the corium–concrete interface, due to the pressure of the released gases.
- Convective flow in the corium pool and the repartition of convective heat exchange coefficients. Nevertheless, recent simulant material tests (Journeau and Haquet, 2009) indicate that the transition from the anisotropic natural convection regime to the isotropic forced convection regime occurs at superficial gas velocities lower than those occurring during MCCI.
- Along with the average gas velocity, another difference between the two types of concretes is the manner in which gas is released out of concrete. For silica-rich concretes, the gas is mainly generated in the mortar (Fig. 16), and is thus transported to the pool at discrete locations between the gravel. For limestone, carbon dioxide is liberated by the decomposition of $CaCO_3$ both in the gravel and in the mortar, leading to a homogeneous gas flow distribution. This difference may also affect the possibility of gas bypass through burned concrete cracks.

6.1.2. Corium–concrete melting temperatures

Siliceous concretes liquidus temperature is generally lower than that of limestone-rich concretes. For instance, computations with GEMINI2 and the NUCLEA database (Cheynet et al., 2004) give a liquidus temperature of 2000 K for the silica-rich VB–U5 concrete while it is of 2300 K for the limestone-rich VB–U6 concrete. But, due to the presence of magnesium carbonate in the CCI-2 concrete, its liquidus temperature is lowered to 2000 K. So, neither the liquidus temperature, nor an ablation temperature – which is arbitrarily defined at a given fraction of liquid, usually between 30% and 50% – discriminates between the concretes exhibiting an isotropic ablation behaviour and the others.

On the opposite, the pseudobinary phase diagrams have a different shape depending for these two types of concretes. For limestone-rich concretes (Fig. 27), the corium–concrete pseudobinary phase diagram has a eutectic valley with a minimum in the liquidus for 70–80 wt.% of concrete. This means that the contact with corium tends to lower the melting temperature of concrete (by 100–200 K). For the silica-rich concretes (Fig. 28), the phase diagram presents a plateau but no eutectic valley. For these concretes, there is no reduction in melting temperature to the mixing of concrete with corium.

For limestone concrete, the pool liquidus temperature becomes very close to the concrete liquidus for a 40 wt.% of concrete and then decrease up to a minimum around a fraction of 80 wt.% whereas the pool liquidus temperature is always greater than concrete liquidus temperature for siliceous concrete. Note that similar conclusion can be conducted with a different threshold on liquid fraction to fix the interface temperature at a different value.

If we postulate that the sidewall crust is not stable, the melted concrete could progressively mix with the corium pool and the so-

lid debris (potentially enriched in refractory species) could accumulate at the bottom part of the pool due to their density. If we assume two different interface temperatures, respectively, for bottom and side walls for siliceous concrete, it will introduce a large dissymmetry in the convection patterns.

6.1.3. Gravel degradation

Limestone aggregate loses its mechanical strength due to decarbonation around 1000 K. On the opposite, quartz (the most common crystal of silica) melts only at 2000 K. Unmelted silica aggregates have been observed (Journeau et al., 2007a; Farmer, 2007) inside the corium pools (Fig. 13).

These silica aggregates, lighter than the liquid corium, can form cold sources in the pool bulk and enhance, near the interfaces, the formation of thick crusts of corium (cf. §4.2) in the case of the silica-rich concretes.

Post-test SEM-EDX analyses of the VULCANO tests with silica-rich concretes have also shown that the measured local corium compositions correspond to a mixing of the corium with mortar. The chemical composition of the mortar (cement + water + sand) and of the concrete (mortar + gravel) are close in the case of concretes rich in limestone, whereas they are significantly different for the concretes rich in silica: the temperatures of liquidus for the mortar and the concrete are, respectively, 1600 and 2000 K for the concrete used in VB–U4, VB–U5 and CCI-3.

6.1.4. Concrete shrinkage

Solid carbonate aggregates have a significantly larger molar volume than their molten oxides. So, upon heating, after decarbonation and melting, the volume of the molten concrete is significantly smaller than that of the initial cold concrete. There is thus a possibility to form cavities between the corium crust and the molten limestone-rich concrete. In this case, the possible crusts on the bottom interface will be much less stable above a limestone-rich concrete than for a silica-rich concrete, the volume of which does not significantly vary at melting.

6.1.5. Molten concrete transport properties

Silica tends to form networks in the melt. The presence of these networks in the molten concrete tends to increase the viscosity (Ramacciotti et al., 2001). The presence of silica in the corium–concrete mixture thus will increase its viscosity and will decrease the heat transfer coefficients, in case of heterogeneity in the pool it can bring to a change of mode of recirculation of the liquid and solid phases. Nevertheless, this effect will not be effective until a sufficient proportion of concrete has been mixed with the corium.

The presence of silica will also reduce the chemical species diffusion coefficient in the molten concrete (and to a lower extent in the corium–concrete mixtures). This coefficient controls the dissolution of the corium crust by molten concrete and could affect the melting time of crusts at the interface.

6.2. Separate effect tests

Due to the experimental constraints related to the prototypic corium tests at high temperature, it appears illusory to be able to observe directly the phenomena causing this anisotropy. This is why we recommended (Journeau et al., 2008) to launch separate effect tests with prototypic corium and concretes, the formulation of which will aim at differing from one of the concretes of reference by only few of the aspects that we listed above. It is expected to be able to determine which parameter have a discriminating influence on the concrete ablation shape. The first test of this series is to be performed with a concrete made with clinker aggregates. Clinker is produced in cement kilns and is an alumino-silicate with almost no carbonates. A concrete composition has been chosen so that the molten concrete composition is close to that of limestone-rich concrete while the gas content is close to that of the silica-rich concrete *F*. Other differences nevertheless exist between this concrete and contrete *G*: the clinker aggregate do not shrink and are not destroyed at medium temperatures as limestone. According to the results of this test, a new concrete composition will be selected in order to narrow even more the list of possible causes of the observed differences, with the aim of determining the cause(s) of the observed anisotropy/isotropy.

Additional simulant fluid experiments will then likely have to address the relevant thermal–hydraulic issues or interface description (temperature, position, crust thickness evolution...) with more precise instrumentation.

This combination of experiments, to be performed within the SARNET2 Joint Programme of Activities on Molten Core–Concrete Interaction (Journeau et al., 2009) should provide the necessary database to build a predictive ablation domain, which will eventually be verified with a blind test on a new concrete composition.

7. Conclusions

Within the VULCANO VB test series, three experiments have been conducted in which two different corium compositions have interacted for more than 2 h with two typical reactor pit basemat concretes. The major finding of these tests as well as of the tests conducted in parallel at ANL is that, although the ablation is roughly isotropic for limestone-rich concretes, it is significantly more pronounced towards the sides than towards the bottom for silica-rich concretes.

Post Test Examinations showed that, for the two tests with silica-rich concrete, the corium actually mixed with mortar (mixture of cement and sand) and not concrete (mixture of cement, sand and gravel) as if the silica gravel had not mixed with the pool. It also showed convective patterns between volumes of melt with different fractions of $(U,Zr)O_2$.

Post Test Calculations showed that, when the ratio of axial to radial ablation is a posteriori fixed, our models are able to describe the heat and mass transfer occurring during MCCI. It also appeared that the deposited crusts must have the composition of the melt rather than being macrosegregated.

At the time of the writing, it is still not possible to propose a comprehensive modeling of MCCI that could predict the observed anisotropies. A list of differences between silica-rich and limestone-rich concretes have been established. In order to determine which of these differences causes the observed anisotropy, it has been proposed to use analytic concretes for Separate Effect Tests in VULCANO in order to determine which phenomenon is responsible for the anisotropic ablation of silica-rich concretes. A first step will be the use of clinker-based concrete which will be rich in calcium oxide but poor in carbon dioxide, in order to assess the effect of gas releases. These prototypic corium tests, coupled with simulant material experiments will form the SARNET2 joint European experimental program for the study of the role of concrete nature on the MCCI ablation profiles.

Acknowledgments

The works and efforts of the whole PLINIUS team are gratefully acknowledged.

The VULCANO program is realized within a national collaboration on MCCI between CEA, IRSN and EDF.

The presented experiments were part of the SARNET Severe Accident Research Network (FP6-EURATOM Contract FI6O-CT-2004-509065) total program of activities.

Appendix A. Appendix: Solidification around silica gravel

Unmelted silica gravel from the concrete has been found entrapped in corium (Fig. 13), mainly in the vicinity of the pool boundaries. This is due to the fact that concrete is an heterogeneous material, made of cement, sand, gravel and water. The mortar (mixture of cement, sand and water) will be first dehydrated and will melt around 1573 K, while the fusion temperature of silica gravel is around 2000 K.

So, the following processes could take place: melting of mortar could liberate solid silica aggregates. As these aggregates are lighter than corium they would tend to rise in corium. Heat exchange between corium and gravel can lead to the melting of the gravel and the cooling of surrounding corium, increasing the initial crust thickness (see Table 7 for crust characteristic dimensions).

This can be modeled analytically, considering a spherical silica particle, extending the works of Kerr (1994b). The notations used in this analysis are presented in Fig. 29.

Equating the heat flux needed to heat and melt a silica gravel and the conductive heat flux in the molten silica layer of thickness e gives:

$$V_{Si}\rho_{Si}\left[H_{Si}+c_{p,Si}(T_{m,Si}-T_m)\right]=k_{m,Si}\frac{T_0-T_{m,Si}}{h_{Si}} \tag{6}$$

where V_{Si} is the silica melting rate.

Equilibrium between viscous and buoyancy forces in the molten silica layer gives (using the geometrical notations of Fig. 30):

$$\frac{\mu_{m,Si}U}{h_{Si}^2}=g(\rho_0-\rho_{m,Si})\sin\beta \tag{7}$$

where U is the characteristic velocity of the molten layer Archimedean rise.

At the angular position β, conservation of mass gives:

$$2\pi R_{Si}\sin\beta V_{Si}=\frac{d}{dz}(2\pi R_{Si}\sin\beta U h_{Si}) \tag{8}$$

where $z = R_{Si}\beta$ is the curvilinear abscissa.

Replacing V_{Si} by its expression from Eq. (6) and U by its value deduced from Eq. (7), Eq. (8) can be written as:

$$a\sin^{5/3}\beta\, d\beta = d(e^3\sin^2\beta)(e^3\sin^2\beta)^{1/3} \tag{9}$$

where

$$a=\frac{k_{m,Si}(T_0-T_{m,Si})\mu_{m,Si}R_{Si}}{g(\rho_0-\rho_{m,Si})\rho_{Si}[H_{Si}+c_{p,Si}(T_{m,Si}-T_m)]} \tag{10}$$

The thickness of the molten layer at the angle β is thus obtained by integration:

$$h_{Si}=\sqrt[4]{\frac{4}{3}a\frac{\int_0^\beta\sin^{5/3}\beta'd\beta'}{\sin^{8/3}\beta}} \tag{11}$$

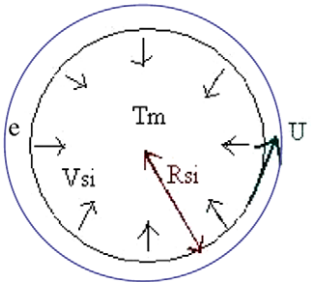

Fig. 29. Notations used for the study of a melting silica sphere.

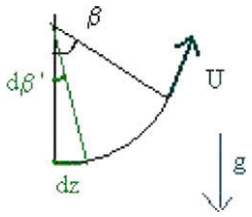

Fig. 30. Geometrical notations for the molten silica layer.

The fusion rate can be written as:

$$V_{Si}=bf(\beta) \tag{12}$$

where:

$$b=\left(\frac{k_{m,Si}(T_0-T_{m,Si})}{\rho_{Si}[H_{Si}+c_{p,Si}(T_{m,Si}-T_m)]}\right)^{3/4}\left(\frac{3}{4}\frac{g(\rho_0-\rho_{m,Si})}{\mu_m R_{Si}}\right)^{1/4} \tag{13}$$

and

$$f(\beta)=\left(\frac{\int_0^\beta\sin^{5/3}\beta'd\beta'}{\sin^{8/3}\beta}\right)^{-1/4} \tag{14}$$

Numerical integration of the function f gives the average fusion rate as:

$$V_{Si,average}=0.92b \tag{15}$$

The thickness of corium which is solidified due to the heat exchange with the gravel is estimated by equating the heat fluxes in the silica and in the corium during the time $\tau_{fusion} = R_{Si}/V_{Si,\,average}$ necessary to melt a gravel:

$$\frac{h_c}{\tau_{fusion}}\rho_0[H_0+c_{p0}(T_0-T_{liq})]=V_{Si,\,average}\rho_{Si}[H_{Si}+c_{p,Si}(T_{m,Si}-T_m)] \tag{16}$$

For a 8-mm radius particle (gravel in the considered concrete is sieved with a 16 mm-mesh), about 12 mm of corium are solidified. The solidification time is estimated, for VB–U5 configurations to 60 s, i.e. an average fusion rate of 45 cm/h. In summary, the presence of floating gravel can cause the formation of an extra centimetre of crust, which will increase the time for the eventual remelting of this crust. It must be stressed that this phenomenon is particular of siliceous aggregates. In contrast, calcium carbonate aggregates are transformed into powder at temperatures around 1000 K due to decarbonation and cannot provide such mechanism.

References

AFNOR, 2001. Eurocode 2: Design of concrete structures and national application document – Part 1 and 2: General Rules: Structural Fire Design. French standard XP ENV 1992-1-2. AFNOR, Paris.

Alsmeyer, H. et al., 1995. Molten Corium/Concrete Interaction and Corium Coolability – A State of the Art Report. Report EUR 16649. European Commission, Luxembourg.

Alsmeyer, H., Miassoedov, A. Cranga, M., Fabianelli, R., Ivanov, I., Doubleva, G., 2005. The COMET-L1 experiment on long-term concrete erosion and surface flooding, In: Proc. Nureth 11, Avignon, France.

Alsmeyer, H., Cron, T., Fluhrer, B., Messemer, G., Miassoedov, A., Schmidt-Stiefel, S., Wenz, T., 2006. The COMET-L3 Experiment on Long-Term Melt–Concrete Interaction and Cooling by Surface Flooding. FZKA 7244.

Azarian, G., Kursawe, H.M., Nie, M., Fischer, M., Eyink, J., Stoudt, R.H., 2004. EPR severe accident threats and mitigation. In: Proc. ICAPP'04. Pittsburgh, PA.

Bakardjieva, S., Barrachin, M., Bechta, S., Bottomley, D., Brissonneau, L., Cheynet, B., Fischer, E., Journeau, C., Kiselova, M., Mezentseva, L.,Piluso, P., Wiss, T., 2008, Improvement of the European thermodynamic database NUCLEA in the frame of EU-funded experiments. In: Proc. ERMSAR. Nesseber, Bulgaria.

Bradley, D.R., Gardner D.R., Brockmann J.E., Griffith R.O., 1993. CORCON-MOD3: An Integrated Computer Model for Analysis of Molten Core–Concrete Interactions. NUREG Report CR-5843, US Nuclear Regulatory Commission.

Blose, R.E., Powers, D.A., Copus, E.R., Brockmann, J.E., Simpson, R.B., Lucero, D.A., 1993. Core–concrete Interactions with Overlying Water Pools – The WETCOR-1 Test. Sandia Nat. Lab. Report NUREG/CR-5907, SAND92-1563.

Bogatov, S.A., Borovoi, A.A., Gavrilov, S.L., et al., 2007, Database on the location and status of nuclear fuel at unit4 of chernobyl NPP before and after the accident. Preprint of RRC Kurchatov Institute, vol. 130, 11/2.

Campbell-Allen, D., Desai, P., 1967. The influence of aggregate on the behaviour of concrete at elevated temperatures. Nucl. Eng. Des. 6, 65–77.

Carénini, L., Haquet, J.F., Journeau, C., 2007, Crust formation and dissolution during corium–concrete interaction. In: Proc. ICAPP'07. Nice, France.

Castellote, M., Alonso, C., Andrade, C., Turrillas, X., Campo, J., 2004. Composition and microstructural changes of cement pastes upon heating, as studied by neutron diffraction. Cem. Concr. Res. 34, 1633–1644.

Cheynet, B., Chaud, P., Chevalier, P.Y., Fisher, E., Masson, P.M., Mignanelli, M., 2004. NUCLEA Propriétés dynamiques et équilibres de phases dans les systèmes d'intérêt nucléaire. Journal de Physique IV 113, 61–64.

Cognet, G., Laffont, G., Jégou, C., Pierre, J., Journeau, C., Cranga, M., Sudreau, F., 2000. The VULCANO ex-vessel programme. Wiss. Ber. FZKA 6475, 156–168.

Copus, E.R., Blose, R.E., Brockmann, J.E., Gomez, R.D., Lucero, D.A., 1989. Core–Concrete Interactions using Molten Steel with Zirconium on a Basaltic Basemat: The SURC-4 Experiment. Sandia National Lab. Report NUREG/CR-4994, SAND87-2008.

Copus, E.R., Blose, R.E., Brockmann, J.E., Simpson, R.B., Lucero, D.A., 1990. Core–Concrete Interactions using Molten UO2 with Zirconium on a Basaltic Basemat: The SURC-2 Experiment. Sandia Nat. Lab. Report NUREG/CR-5564, SAND90-1022.

Copus, E.R., Blose, R.E., Brockmann, J.E., Simpson, R.B., Lucero, D.A., 1992. Core–Concrete Interactions Using Molten Urania With Zirconium on a Limestone Concrete Basemat. The SURC-1 Experiment, Sandia National Lab. Report NUREG/CR-5443.

Cranga, M., Fabianelli, R., Jacq, F., Barrachin, M., Duval, F., 2005. The MEDICIS code, a versatile tool for MCCI modeling. In: Proceedings of ICAPP05. Seoul, Korea.

Cranga, M., Mun, M, Michel, B., Duval, F., Barrachin, M., 2008. Interpretation of real material experiments in homogeneous oxidic pool with the ASTEC/MEDICIS code. In: Proc. of ICAPP'09. Anaheim, CA, USA.

Farmer, M.T., Spencer, B.W., Kilsdonk, D.J., Aeschlimann, R.W., 1999. Status of large scale MACE core coolability experiments. In: Proc. OECD Workshop on Ex-Vessel Debris Coolability. Karlsruhe, Germany.

Farmer, M., Spencer, B.W., 1999b. Status of the CORQUENCH model for calculation of ex-vessel corium coolability by an overlying water layer. In: Proc. OECD Workshop Ex-vessel Debris Coolability. Karlsruhe, Germany.

Farmer, M.T., Lomperski, S., Basu, S., 2004. Results of reactor materials experiments investigating 2D-core–concrete interaction and debris coolability. In: Proc. ICAPP'04. Pittsburgh, PA.

Farmer, M.T., Lomperski, S., Basu, S., 2005, The results of the CCI-2 reactor materials experiment investigating 2D-core–concrete interaction and debris coolability. In: Proc. NURETH-11. Avignon, France.

Farmer, M.T., Lomperski, S., Basu, S., 2006. The results of the CCI-3 reactor materials experiment investigating 2D-core–concrete interaction and debris coolability with a siliceous concrete crucible. In: Proc. ICAPP'06. Reno, NV.

Farmer, M.T., 2007, A summary of findings from lelt coolability and concrete interaction (MCCI) program. In: Proc. ICAPP'07. Nice, France.

Fischer, M., 2004. The severe accident mitigation concept and the design measures for core melt retention of the European pressurized reactor (EPR). Nucl. Eng. Des. 230, 169–170.

Foit, J.J., 1997. Modelling oxidic molten core–concrete interaction in WECHSL. Nucl. Eng. Des. 170, 73–79.

Frolov, K.N., 2004. Diffusion chimique à l'état liquide dans des bains silicates. Application aux accidents graves de réacteurs nucléaires. Ph.D Thesis, Université Joseph Fourier, Grenoble, France.

Gatt, J.-M. Buffe L., Marchand, O., 1995. Numerical modelling of the corium–substratum system. In: Proc. 13th Int. Conf. Structural Mech. Reactor Technol. (SMIRT 13), Porto Allegre, Brazil.

Georgali, B., Tsakiridis, P.E., 2005. Microstructure of fire-damaged concrete – a case study. Cem. Concr. Compos. 27, 255–259.

Jégou, C., Cognet, G., Roubaud, A., Gatt, J.M., Laffont, G., Kassabjo, F., 1998. Plasma transferred arc rotary furnace for corium melting. J. High Temp. Mater. Proc. 1, 409–420.

Journeau, C., Sudreau, F., Gatt, J.M., Cognet, G., 1999. Thermal, physico-chemical and rheological boundary layers in multi-component oxidic melt spreads. Int. J. Therm. Sci. 38, 879–891.

Journeau, C., Sudreau, F., Magne, S., Cognet, G., 2001. Physico-chemical analyses and solidification path reconstruction of multi-component oxidic melt spreads. Mater. Sci. Eng. 299A, 249–266.

Journeau, C., Jégou, C., Monerris, J., Piluso, P., Frolov, K., Petrov, Yu. B., Rybka, R., 2003a. Phase macrosegregation during the slow solidification of prototypic corium, In: Proc. NURETH-10, Seoul, Korea, October 5–9, 2003.

Journeau, C., Boccaccio, E., Brayer, C., Cognet, G., Haquet, J.F., Jégou, C., Piluso, P., Monerris, J., 2003b. Ex-vessel corium spreading: results from the VULCANO spreading tests. Nucl. Eng. Des. 223, 75–102.

Journeau, C., Boccaccio, E., Bonnet, J.M., Fouquart, P., Godin-Jacqmin, L., Haquet, J.F., Magallon, D., Malaval, S., Mwamba, K., Piluso, P., Saldo, V., 2005. Severe accident research at the PLINIUS prototypic corium platform. In: Proc. ICAPP'05. Seoul, Korea.

Journeau, C., Alsmeyer, H., 2006. Validation of the COMET bottom-flooding core–catcher with prototypic corium. In: Proc. ICAPP'06. Reno, NV.

Journeau, C., Piluso, P., Haquet, J.F., Brissonneau, L., Aubert-Saldo, V., 2007a. Behaviour of nuclear reactor pit concretes under severe accident conditions. In: Proc. CONSEC '07, Concrete under Severe Conditions. Tours, France.

Journeau, C., Piluso, P., Haquet, J.F., Saretta, S., Boccaccio, E., Bonnet, J.M., 2007b. Oxide–metal corium–concrete interaction test in the VULCANO facility. In: Proc. ICAPP'07. Nice, France.

Journeau, C., Haquet, J.-F., 2009. Convection heat transfer anisotropy in a bubbling viscous pool – application to molten core–concrete interaction. Nucl. Eng. Des. 239, 389–394.

Journeau, C., Haquet, J.-F., Piluso, P., Bonnet, J.-M., 2008. Differences between silica and limestone concretes that may affect their interaction with corium. In: Proc. ICAPP 2008. Anaheim, CA.

Journeau , C., Cranga, M., Foit, J., Ma, W., Grudev, P., 2009. A European joint workplan on molten core–concrete interaction. In: Proc. ICAPP'09. Tokyo, Japan.

Kerr, R.C., 1994a. Dissolving driven by vigourous compositional convection. J. Fluid Mech. 280, 287–302.

Kerr, R.C., 1994b. Melting driven by vigorous compositional convection. J. Fluid Mech. 280, 255–285.

Khoury, G.A., 2000. Effect of fire on concrete and concrete structures. Prog. Struct. Eng. Mater. 2, 429–447.

Loulou, T., Artyukhin, E.A., Bardon, J.P., 1999. Estimation of thermal contact resistance during the first stages of metal solidification. Int. J. Heat Mass Transfer 42, 2119–2142.

Maruyama, Y., Kojima, Y., Tahara, M., Nagasaka, H., Kato, M., Kolodeshnikov, A.A., Zhdanov, V.S., Vassiliev, Yu.S., 2006. A study on concrete degradation during molten core/concrete interactions. Nucl. Eng. Des. 236, 2237–2244.

Mungall, J.E., 2002. Empirical models relating viscosity and tracer diffusion in magmatic silicate melts. Geochim. Cosmochim. Acta 66, 125–143.

Nie, M., 2005., Temporary melt retention in the reactor pit of the European pressurized water reactor (EPR). Eng. Dr. Thesis, University of Stuttgart, Germany.

Noumouwé, A., 1995. Effet des Hautes Températures (20–600 °C) sur le Béton, Ph.D Thesis, Institut National des Sciences Appliquées, Lyon, France.

Ramacciotti, M., Sudreau, F., Journeau, C., Cognet, G., 2001. Viscosity models for corium melts. Nucl. Eng. Des. 204, 377–389.

Sdouz, G., Mayrhofer, R., Alsmeyer, H., Cron, T., Fluhrer, B., Foit, J., Messemer, G., Miassoedov, A., Schmidt–Stiefel, S., Wenz, T., 2006. The COMET-L2 experiment on long-term MCCI with steel melt, FZKA 7214.

Seiler, J.M., Froment, K., 2000. Material effects on multiphase phenomena in late phases of severe accidents of nuclear reactor. Multiphase Sci. Technol. 12, 117–257.

Sevón T. et al., 2007. HECLoA–2 Experiment on Melt–Concrete Interactions, VTT Technical Research Centre of Finland Research Report VTT–R–11203-07.

Shin, K.-Y., Kim, S.-B., Kim, J.-H., Chung, M., JUNG, P.-S., 2002. Thermo-physical properties and transient heat transfer of concrete at elevated temperatures. Nucl. Eng. Des. 212, 233–241.

Spindler, B., Tourniaire, B., Vandroux, S., Seiler, J.M., Gubaidulin, A., 2005. MCCI analysis based on the phase segregation model with application in the TOLBIAC ICB code. In: Proc. NURETH-11. Avignon, France.

Thompson, D.H., Farmer, M.T., Fink, J.K., Armstrong, D.R., Spencer, B.W., 1997. Compilation, Analysis and Interaction of ACE Phase C and MACE Experimental Data. Report ACEX TR-C-14, Argonne National Laboratory, Chicago, IL.

Trambauer, K., Schwinges, B., 2007. Evaluation of research priorities in the frame of SARNET. In: Proc. Euro. Review Mtg on Severe Accident Res. ERMSAR-2007. Karlsruhe, Germany.

Urbain, G., Bottinga, Y., Richet, P., 1982. Viscosity of liquid silica, silicates and alumino-silicates. Geochim. Cosmochim. Acta 46, 1061–1072.

Veteau, J.M., 2005. Experimental investigation of interface conditions between oxidic melt and ablating concrete during MCCI by means of simulating material experiments: the Artemis program. In: Proc. 11. Nureth 11. Avignon, France.

Wriedt, H.A., 1990. The O–Si (Oxygen–Silicon) system. Bull. Alloy Phase Diagrams 11, 43–61.